A modified scheme for wind farm parameterization in WRF considering the impact of the floating wind turbine on waves

Shaokun Deng[1], Shengmu Yang[2], Shengli Chen[1,]*, Xuefeng Yang[1], and Shanshan Cui[1]

1 Institute for Ocean Engineering, Shenzhen International Graduate School, Tsinghua University, Shenzhen, China

2 College of Meteorology and Oceanography, National University of Defense Technology, Changsha, China

Corresponding author: Shengli Chen (shenglichen@sz.tsinghua.edu.cn)

Key Points:

- A wind turbine module is implemented in the spectral wave model that accounts for the energy dissipation caused by the inertial forces.
- High-resolution wave model is replaced by a machine learning model and implemented in the Weather Research and Forecasting model.
- Consideration of turbine-induced changes in momentum flux is key to the parameterizing floating wind farms.

Abstract

A new scheme is developed for floating wind farm parameterization (FWFP) in the Weather Research and Forecasting (WRF) model. The impacts of the side columns of a semi-submersible floating wind turbine on waves are firstly parameterized in the spectral wave model (SWAN) where the key idea is to consider both inertial and drag forces on side columns. A machine learning model is trained using results of idealized high-resolution SWAN simulations and then implemented in the WRF to calculate the frictional velocity at the turbine site. This frictional velocity is passed to the Fitch wind farm parameterization to form the FWFP. The difference between our new scheme and the original Fitch scheme in a realistic case is investigated using a coupled atmosphere-wave model. Results indicate that the FWFP can increase total power output of wind farms by over 5% in the high wind speed stage due to significant wave height attenuation caused by large-scale floating turbines. The turbulent kinetic energy decreases within the wind farm, with the greatest drop of 0.4 m^2s^{-2} at the top of the turbine. The impact of the new scheme can spread to the top of the atmospheric boundary layer. The proposed new scheme will help forecast wind energy and explore the potential impacts of large floating wind farms.

Plain Language Summary

The global offshore wind power development is moving from offshore to deeper waters, where floating offshore wind turbines have advantage over bottom fixed offshore wind turbines. However, current wind farm parameterization schemes in mesoscale models are not applicable to floating turbines. In this study, we propose a floating wind farm parameterization scheme that accounts for the attenuation of the significant wave height by floating turbines. By comparing with the original wind farm parameterization, the results indicate that the new scheme has a significant impact on the wind speed deficits as well as the turbulent kinetic energy.

1. Introduction

Wind farms could have a great impact on the environment, including wind speed, turbulent kinetic energy (TKE), temperature, humidity, and other atmospheric parameters (Fitch, 2015; Siedersleben et al., 2018). This impact is not suitable to be investigated with the computational fluid dynamics (CFD) models and large-eddy simulation (LES) model due to great computational expense and feedback effects that cannot be captured by high-resolution non-meteorological microscale models alone. Engineering wake models also lack the relevant physical processes that are important for large scale wind farms or wind farm clusters with hundreds of turbines or more (Emeis, 2010). Currently, an important tool for studying wind farms is mesoscale models with a wind farm parameterization. In mesoscale models, there are two different methods to parameterize the wind farm: implicit and explicit methods. Previous results have shown that explicit methods represent the wind farm effects in a more physically consistent way and lead to more realistic results (Fitch et al., 2013; Fitch, 2015). In addition, the explicit methods have the advantage of accounting for the interaction of wind speeds with the surface below (Du et al., 2017; Vanderwende & Lundquist, 2016). The explicit methods parameterize the wind farm effect as a momentum sink on the mean flow and as a source of TKE (Abkar and Porté-Agel, 2015; Blahak et al., 2010; Fitch et al., 2012; Pan & Archer, 2018; Redfern et al., 2019; Volker et al., 2015). Most of parameterizations are conducted in the free, open-source Weather Research and Forecasting (WRF) model, which already includes the Fitch wind farm parameterization in its release (Fitch et al., 2012).

The installed capacity of offshore wind energy has been continuously increasing (Diaz et al., 2020). Unlike onshore wind farms, offshore wind farms affect the waves and thus the roughness length of the surrounding surface. Changes in the roughness length in turn affect the wind field through momentum transfer between the atmosphere and the waves, and previous studies have found that an impact of the wave field on the wind field can reach into the height of the turbine (AlSam et al., 2015; Jenkins et al., 2012; Kalvig et al., 2014; Paskyabi et al., 2014; ; Porchetta et al., 2021; Wu et al., 2020; Yang et al., 2014; Zou et al., 2018). There is a complex interaction between wind and waves. Wind turbines influence waves in two ways: 1) through a reduced wind stress as a consequence of the kinetic energy extraction by the turbines (Christensen et al., 2013) and 2) through the interaction with the wind turbine pole due to reflection, diffraction and drag dissipation. The global offshore wind power development is moving from offshore to deeper waters, where floating offshore wind turbines have advantage over bottom fixed offshore wind turbines in water depths greater than 50 m (Diaz et al., 2020; Roddier et al., 2010). Floating offshore wind turbines can have a substantial impact on waves due to floating platforms, which in turn leads to major changes in roughness length of ocean surface, requiring modifications of the current wind farm parameterization scheme used in mesoscale meteorological models.

The influence of wind farm structures on waves has been investigated in only a few studies. Ponce de Leon et al. (2011) used the Simulation WAves Nearshore (SWAN) model to study the impact of an offshore wind farm on nearby waves. Since the monopile foundations included in their study could not realistically be resolved, each monopile foundation was represented as a dry point (land) in the model. They found that the simulated monopiles acted as obstacles blocking the propagation of wave energy and slightly altering the wave direction. Alari & Raudsepp (2012) found that the impact of the wind turbine on the significant wave height (SWH) was very marginal, with changes of the SWH smaller than 1% at areas shallower than 10 m depth. Molen et al. (2014) conducted sensitivity experiments to study the influence of turbine spacing and size of wind farm on the SWH, and found that the SWH could be reduced by up to 9.58%. McCombs et al. (2014) evaluated the impact of an offshore wind farm on waves in Lake Ontario using a coupled wave-hydrodynamic model. In the study, the offshore wind farm was simulated by applying a transmission coefficient in the wave model and adding a quadratic friction term to the momentum equations of the hydrodynamic model in the area of the proposed wind farm. The results indicated that the wave heights in coastal areas will be minimally affected with changes of SWH predicted to be less than 3%.

These previous studies simulate the wind turbine in the model as a dry grid point, which has two limitations, 1) the model resolution is too high to implement for large-scale offshore wind farm scenarios, 2) it can only represent the diffraction effects, however, wave forces include drag and inertial forces (Isaacson, 1979; Morison et al., 1950). By parameterizing both the drag and inertial forces in the numerical model, the impact of the offshore wind turbine/farm on the waves can be analyzed more accurately. Previous studies also discussed the impact of bottom fixed wind turbines on waves, while the impact of floating offshore wind turbines on waves needs to be re-evaluated due to the significant structural differences between floating and bottom fixed wind turbines.

In this study, a floating offshore wind farms parameterization scheme in the WRF Model is developed to represent the effect of the offshore wind farm on surface waves. In Section 2, the wave energy dissipation due to the inertial forces of waves is implemented in SWAN. The model conFigureuration and results of high-resolution idealized simulations are presented in Section 3. In Section 4, we propose a machine learning module used to fit the effect of wave inertial forcings represented in high-resolution SWAN simulations. Section 5 describes how the floating wind farm parameterization scheme is implemented in the WRF, and presents the results and the analysis of the wind speed deficit, power output, and the influence of the new scheme on the turbulent kinetic energy. The conclusion is given in Section 6.

2. Parameterization of the wave inertial force in SWAN

2.1 SWAN

SWAN is a third-generation phase-averaged spectral wave model (Booij et al., 1999). The model propagates offshore wave conditions, input at the model boundaries as either integrated parameters or spectra, across a user defined grid of bathymetry to the region of interest. The evolution of the wave energy density spectrum in space and time is calculated by solving the action balance equation. This equation includes source terms for energy input into the model (from wind), dissipation (from white capping and shallow-water effects) and redistribution (via triad and quadruplet interactions). Shallow water and depth-limited processes including refraction, bottom friction and depth-induced breaking are accounted, and diffraction in SWAN is represented by a phase-decoupled approach (Holthuijsen et al., 2003). Further details on the physical processes in SWAN can be found in the SWAN User Manual (The SWAN steam, 2023).

The rate of change of the action density N at a single point is governed by the action balance equation,

$$\frac{\partial N}{\partial t}+\frac{\partial}{\partial x}C_x N+\frac{\partial}{\partial y}C_y N+\frac{\partial}{\partial \sigma}C_\sigma N+\frac{\partial}{\partial \theta}C_\theta N=\frac{S_{tot}}{\sigma} \tag{1}$$

$$N(\sigma,\theta)=\frac{E(\sigma,\theta)}{\sigma} \tag{2}$$

where E is energy density, σ is the relative radian frequency, θ is propagation directions, C_x and C_y are the propagation velocities of action density in two-dimensional geographical space, C_σ and C_θ are the propagation velocities in spectral space, S_{tot} is the non-conservative source/sink term that represents all physical processes which generate, dissipate, or redistribute wave energy.

In the shallow water region, seven basic processes contribute to S_{tot}:

$$S_{tot} = S_{in} + S_{nl3} + S_{nl4} + S_{ds,w} + S_{ds,b} + S_{ds,br} + S_{ds,veg} \tag{3}$$

where S_{in} denotes wave growth by the wind, S_{nl3} and S_{nl4} indicate nonlinear transfer of wave energy through three-wave and four-wave interactions, respectively. The wave decay due to whitecapping, bottom friction, depth-induced wave breaking and vegetation are denoted by $S_{ds,w}$, $S_{ds,b}$, $S_{ds,br}$ and $S_{ds,veg}$, respectively.

2.2 Wave damping due to the inertial forces

SWAN has a function to include wave damping over a vegetation (VEG) field at variable depths. A popular method of expressing the wave dissipation due to vegetation is the cylinder approach suggested by Dalrymple et al. (1984). In this approach, energy losses are calculated as actual work carried out by the vegetation due to plant induced forces acting on the fluid, expressed in terms of a Morison type equation. Two modifications convert the VEG module into the semi-submersible floating wind turbine module. The energy dissipation in each vertical layer is calculated separately, and the total energy dissipation is equal to the sum of the dissipation across all layers up to the still water level (Figure 1). The first modification then is that the module only needs to calculate the results of $S_{veg,3}$ (the red dashed box in Figure 1) and set *d* (column draft depth) to a constant (*d*=20 m is used in this paper).

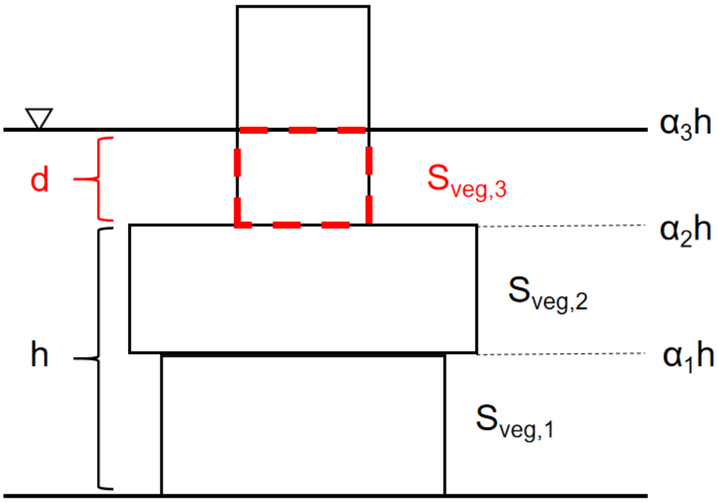

Figure 1. Layer schematization for vegetation

Another important modification of the VEG module concerns the energy dissipation due to wave forces. In the VEG module, the wave force is derived from the drag force in a Morison type equation with the inertial forces neglected. Since the vegetation is assumed to be a cylinder with a small diameter, the drag force is considered to be dominant. However, for the floating offshore wind turbine, the diameter of the cylinder cannot be neglected compared to the wavelength. The wave forces become more complex and require the consideration of inertial forces. The equation for the energy dissipation due to inertial forces can be derived from the work of Morison et al. (1950).

$$D = \int_{-(h+d)}^{-h} F_{iner} \cdot u dz = \int_{-(h+d)}^{-h} C_M \rho \frac{\pi b^2}{4} \frac{\partial u}{\partial t} \cdot u dz \tag{4}$$

where C_M is the inertial force coefficient, b is the cylinder diameter. Based on Kobayashi et al. (1993), the formula for $\partial u / \partial t$ is derived as below

$$u = \frac{gkH}{2\omega} \frac{\cosh[k(h+d+z)]}{\cosh[k(h+d)]} \tag{5}$$

$$\frac{\partial u}{\partial t} = \frac{gkH}{2} \frac{\cosh[k(h+d+z)]}{\cosh[k(h+d)]} [\delta c_2 + (\delta - \varepsilon) c_3] \tag{6}$$

where ω is the wave angular frequency, H is the wave height, k is the wave number, $h+d$ is the water depth, d is the draft depth (Figure 1).

The equations for the other parameters are as follows,

$$\varepsilon = \frac{C_D b H}{9\pi} \cdot c_5 \tag{7}$$

$$\delta = \varepsilon \cdot c_4 \tag{8}$$

$$c_2 = \frac{\sinh kh \sinh[k(h+d)] - kh \tanh kd}{\cosh kd} \tag{9}$$

$$c_3 = k(h+d+z) \tanh[k(h+d+z)] - kd \tanh kd \tag{10}$$

$$c_4 = \frac{2kd + \sinh 2kd}{2k(h+d) + \sinh[2k(h+d)]} \tag{11}$$

$$c_5 = \frac{\sinh 3kd + 9 \sinh kd}{(2kd + \sinh 2kd) \sinh[k(h+d)]} \tag{12}$$

Substitution of Eqs. (5), (6) and (10) into Eq. (4) yields

$$D = \frac{C_M \rho \pi b^2 k (gH)^2}{16\omega \cosh^2[k(h+d)]} [\delta c_2 \frac{\sinh 2kd + 2kd}{4} + (\delta - \varepsilon) \frac{2kd \cosh 2kd - \sinh 2kd - kd \tanh kd (\sinh 2kd + 2kd)}{8}] \tag{13}$$

Substitution of Eqs. (7) and (8) into Eq. (13) yields

$$D = \frac{C_M C_D \rho b^3 k g^2 H^3}{144\omega \cosh^2[k(h+d)]} [c_4 c_5 c_2 \frac{\sinh 2kd + 2kd}{4} + c_5 (c_4 - 1) \frac{2kd \cosh 2kd - \sinh 2kd - kd \tanh kd (\sinh 2kd + 2kd)}{8}] \tag{14}$$

Waves can be described by a joint distribution of wave height, period (or frequency) and direction. A Rayleigh distribution often gives a satisfactory characterization of the random variation in wave height (Mendez & Losada, 2004). The Rayleigh probability density function is related to wave height,

$$H^3 = \int_0^\infty H^3 p(H) dH \tag{15}$$

$$\int_0^\infty H^3 p(H) dH = \frac{3\sqrt{\pi}}{4} H_{rms}^3 \tag{16}$$

where $p(H)$ is the Rayleigh probability density function, H_{rms} is the root-mean-square wave height. Substitution of Eqs. (15) and (16) into Eq. (14) and dividing by the bulk density of the fluid yields

$$D = \frac{C_M C_D b^3 g k N}{144\omega \cosh^2[k(h+d)]} \frac{3\sqrt{\pi}}{4} H_{rms}^3 [c_4 c_5 c_2 \frac{\sinh 2kd + 2kd}{4} + c_5 (c_4 - 1) \frac{2kd \cosh 2kd - \sinh 2kd - kd \tanh kd (\sinh 2kd + 2kd)}{8}] \tag{17}$$

The root-mean-square wave height and the total wave energy have such a relationship, $H_{rms}^2 = 8E_{tot}$, and substituting it into Eq. (17) yields,

$$D = \frac{1}{8}\sqrt{\frac{\pi}{72}}\frac{C_M C_D b^3 gk}{\omega \cosh^2[k(h+d)]}[2c_4c_5c_2(\sinh\ 2kd + 2kd) + c_5(c_4-1)[2kd\cosh 2kd - \sinh\ 2kd - kd\tanh kd(\sinh\ 2kd+2kd)]]E_{tot}^{3/2} \tag{18}$$

Eq. (18) is the equation calculating the energy dissipation due to the inertial force. In the study, the magnitudes of the inertial force and the drag force are calculated and compared for the cylinders with diameters of 10 m and 1 m.

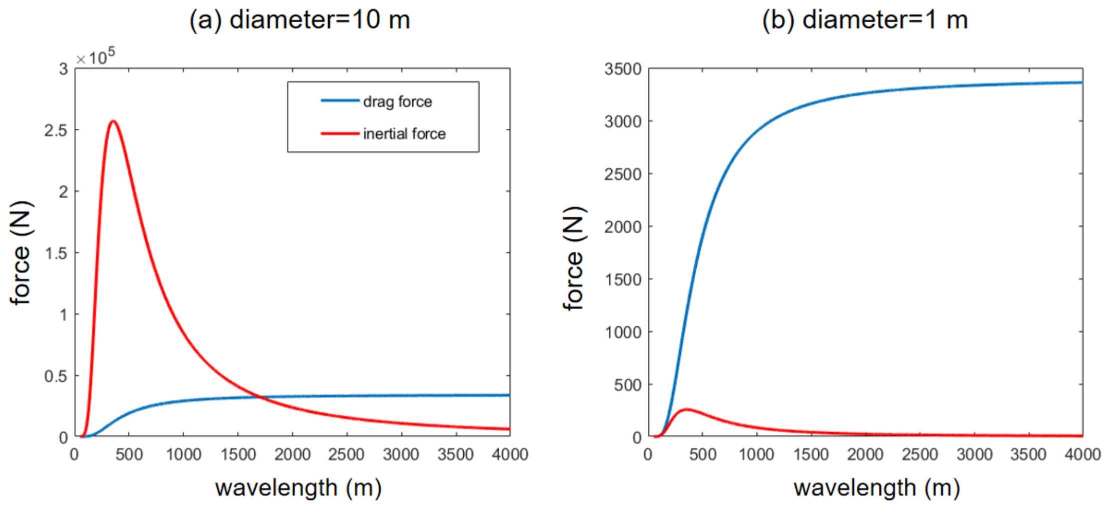

Figure 2. Inertial forces (red solid line) and drag forces (blue solid line) for cylindrical diameters of (a) 10 m and (b) 1 m (incident wave height of 3 m, drag coefficient of 1.2, draft depth of 20 m, water depth of 80 m)

The case is set with the incident SWH of 3 m, the drag coefficient of 1.2, the draft depth of 20 m, and the water depth being 80 m. When the cylinder diameter is 10 m (Figure 2a), the average wavelength of the incident wave is within 1700 m, which makes the inertial force larger than the drag force. However, when the cylinder diameter is 1 m (Figure 2b), the inertial force is always smaller than the drag force. As the wavelength increases (the scale becomes smaller), the drag force becomes larger relative to the inertial force, which is consistent with the assumption of the VEG module that the inertial force could be neglected, but the inertial force can not be ignored for the side column of the floating offshore wind turbine. Thus the VEG module in SWAN is modified to include the inertial force to be applicable for the floating wind turbine.

3. Idealized high-resolution simulations

As shown in Section 2, the floating offshore wind turbine module is developed for SWAN, and its impact on waves is examined using high-resolution numerical experiments in this section.

The rectangular domain of the idealized high-resolution experiments is shown in Figure 3, with 100×200 cells, a horizontal resolution corresponding to the column diameter of 10 m, and a water depth of 50 m. The position of the column is at the center of the computational domain. The incident SWH is 3 m, the mean wave period is 12 s, propagating from east to west, and the shape of the spectra is from the JONSWAP spectrum. Because of the small computational domain, the model uses stationary computation which converges after several time steps.

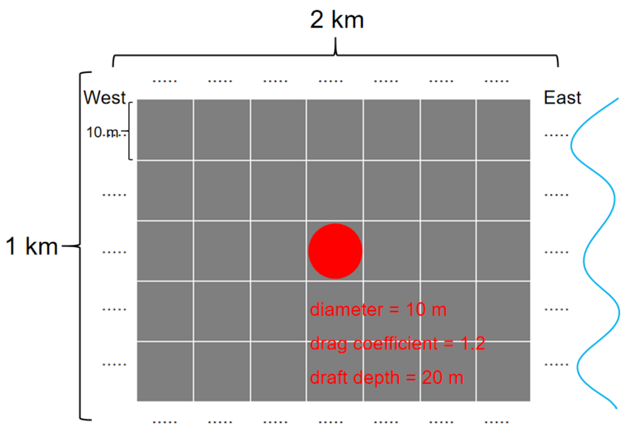

Figure 3. Experimental design of high-resolution idealized simulations (SWH=3 m, mean wave period=12 s, and depth=50 m)

Two experiments are conducted, one to study the influence of the column on the waves caused only by the drag force (ExpDragS), and the other to examine the influence caused by both the drag force and the inertial force (ExpInerS). It can be noted that when the energy dissipation is caused by the drag force only, the SWH attenuation is only ~0.2 m (Figure 4a), and the "wake" phenomenon occurs in the wave field. The angle of the mean wave direction is shifted by about 1° around the column and the horizontal distribution is symmetrical along the axis y=0 (Figure 4d). The mean wave length is increased by about 10 m (Figure 4g). When the inertial forces are taken into account, the energy dissipation is larger, which makes the SWH attenuation more significant, which is about 1.4 m (Figure 4b), indicating an attenuation of 50% SWH. The mean wave direction deviation around the column is also relatively large, reaching about 5° (Figure 4e), and the mean wave length is about 24 m longer (Figure 4i) than that of ExpDragS.

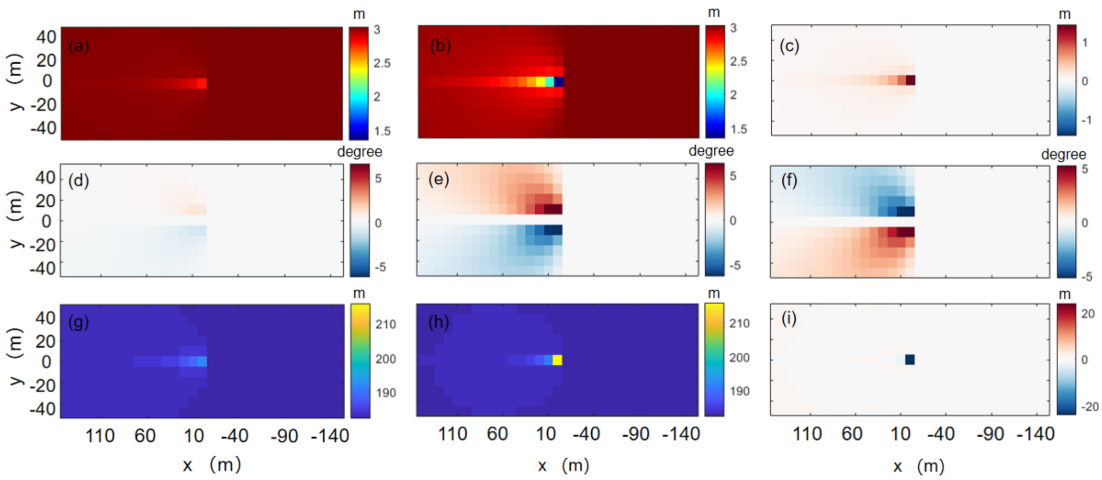

Figure 4. Significant wave height of (a) ExpDragS and (b) ExpInerS, (c) difference in significant wave height, (d) mean wave direction deviation of ExpDragS and (e) ExpInerS, (f) difference in mean wave direction deviation, (g) mean wave length of ExpDragS, and (h) ExpInerS, (i) difference in mean wave length

4. Machine learning parameterization

The results of the idealized high-resolution SWAN simulations in Section 3 show the impact of the floating offshore wind turbine's side columns on the waves, including the SWH attenuation, symmetrical changes of mean wave direction, and an increase in the mean wave length. However, it is computationally expensive to run a ~10 m resolution SWAN model.

The use of machine learning (ML) for better parametrizing unresolved processes in mesoscale and climate models has gained much attention recently (O'Gorman & Dwyer, 2018; Gettelman et al., 2020; Seifert & Rasp, 2020). With the rise of scientific machine learning and its broad application in the geosciences, the design of parametrizations using ML algorithms has become a trend in model development. To build an appropriate model, a large amount of data is needed for training. Nevertheless, the observational data on the impact of the floating offshore wind turbine on waves are scarce. As a result, the outputs of the high-resolution SWAN simulations in Section 3 are employed to train the ML model.

From the equations in Section 2, we can note that when the inertial force coefficient, drag force coefficient, and cylindrical diameter are determined, the energy dissipation caused by the wave force is only related to the water depth, incident SWH, and mean wave period (or peak period). We design a series of ideal experiments with different water depths, incident SWH, and mean wave periods. The SWH is taken from 2 m to 12 m with 1 m interval. The peak wave period is from 7 s to 12 s with an interval of 1 s, and the water depth is selected from 53 m to 98 m with an interval of 5 m. This has a total number of 660 (11 × 6 × 10) experimental groups. We then use these model data to train several machine learning (regression) models with the input of incident SWH, water depth, and peak wave period, and the output of SWH after energy dissipation. These models can be classified into four main categories: linear regression models, tree models, support vector machines (SVM), and Gaussian process regression (GPR). As shown in Figure 5, the GPR model with the Matern 5/2 kernel (covariance) function is the most reasonable, with a minimum root mean square error (RMSE) of 0.0096 m (Figure 5d). The model can be coupled with CFD, LES models and mesoscale meteorological models to predict the effect of the floating offshore wind turbine side columns on waves without the need for high-resolution SWAN simulations.

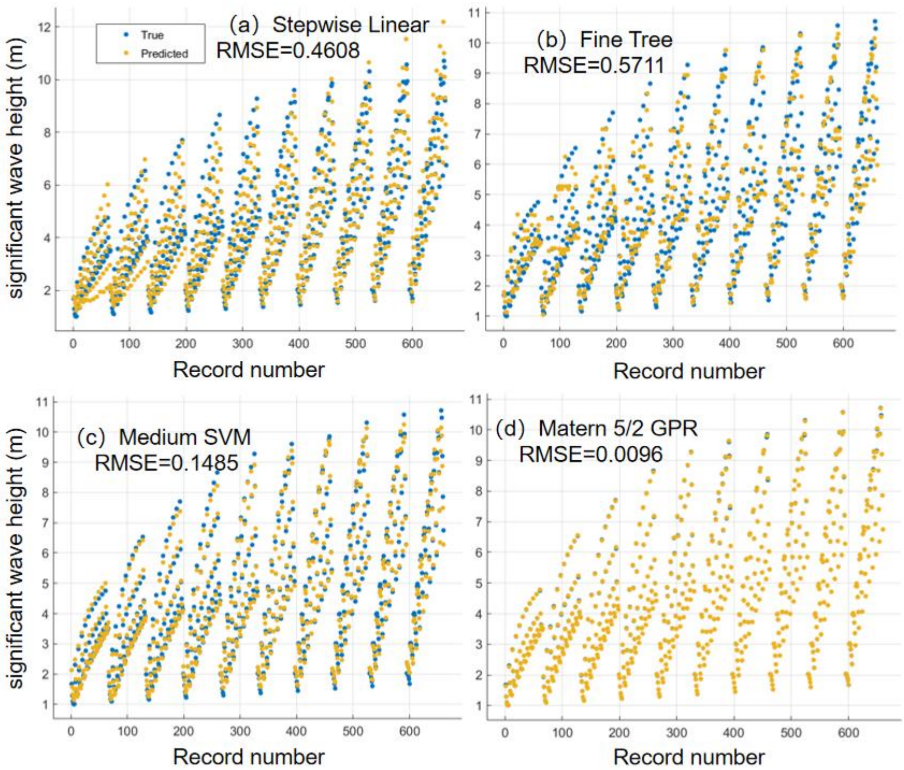

Figure 5. Response results of four typical regression models: (a) Stepwise linear regression (b) Fine tree (c) Medium SVM (d) Matern 5/2 Gaussian process regression

5. Parameterization in a mesoscale model

5.1 Implementation of parameterization in WRF

The Fitch wind-farm parametrization (Fitch et al., 2012), which has been implemented in the WRF model, is the most widely used method to simulate large wind farms. The important point in the derivation of the Fitch equation is that the rate of loss of kinetic energy in the grid cell is equal to the kinetic energy loss due to the wind turbine in the grid,

$$-\frac{1}{2}N_{ij}\Delta x\Delta y\rho C_T|V|_{ijk}^3 A_{ijk} = \Delta x\Delta y(z_{k+1}-z_k)\rho|V|_{ijk}\frac{\partial|V|_{ijk}}{\partial t} \quad (19)$$

where $|V|_{ijk}$ is the horizontal wind speed, N_{ij} is the number of turbines per square meter, ρ is the air density, C_T is the thrust coefficient of a wind turbine, $\Delta x, \Delta y$ are the horizontal grid size in the zonal and meridional directions respectively, z_k is the height at model level k, A_{ijk} is the cross-sectional rotor area of one wind turbine bounded by model levels $k, k+1$ in grid cell i, j.

For a semi-submersible floating wind turbine, the SWH around the turbine is considerably affected. As a result, the roughness of ocean surface nearby is also changed. The change in the kinetic energy due to changes in the momentum flux in the surface layer should be taken into account for the loss of kinetic energy in the grid cell. Therefore, in the simulation with semi-submersible floating wind turbines applied, Eq. (19) can be modified

$$-\frac{1}{2}N_{ij}\Delta x\Delta y[\rho C_T|V|_{ijk}^3 A_{ijk} - \Delta\tau\cdot S|V|_{ijk}(z_{k+1}-z_k)] = \Delta x\Delta y(z_{k+1}-z_k)\rho|V|_{ijk}\frac{\partial|V|_{ijk}}{\partial t} \quad (20)$$

where S is the area occupied by the floating platform. $\Delta\tau = \rho(u_{*,wt}^2 - u_*^2)$ is the change in the momentum flux due to the turbine. $u_{*,wt}$ is the frictional velocity at location of the turbine and u_* is the frictional velocity unaffected by the turbine. A new equation for the momentum tendency term is given as

$$\frac{\partial|V|_{ijk}}{\partial t} = -\frac{N_{ij}[\frac{1}{2}C_T|V|_{ijk}^2 A_{ijk} + (u_{*,wt}^2 - u_*^2)S(z_{k+1}-z_k)]}{(z_{k+1}-z_k)} \quad (21)$$

It should be noted that Eq. (21) applies only to the heights between the bottom of the rotor area and 100 m (top of the surface layer). The momentum flux term in Eq. (21) can be omitted when z_{k+1} is greater than 100 meters. In addition, the new parameterization calculates the momentum tendency below the bottom of the rotor area, i.e., only the momentum flux term is retained in Eq. (21).

The variables exchanged between WRF and SWAN is shown in Figure 6. WRF provides 10-m surface wind (U10, V10) to SWAN, whereas SWAN returns SWH (hwave), peak wave length (lwavep), and peak wave period (pwave) to WRF. This variable exchange is implemented in the WRF model. The trained GPR model needs water depth as the input, thus we implement SWAN to provide water depth to WRF. Specifically, we incorporate the GPR model into the surface layer parameterization module of WRF. As a result, the SWH affected by the floating offshore wind turbine (hwavewt) can be calculated directly in the surface layer parameterization module to obtain the roughness length, frictional velocity, and other variables. The frictional velocity at the location of the wind turbine (ustwt) and the frictional velocity unaffected by the turbine (ust) are input to the existing wind farm parameterization module in WRF to make the parameterization module suitable for floating offshore wind farms.

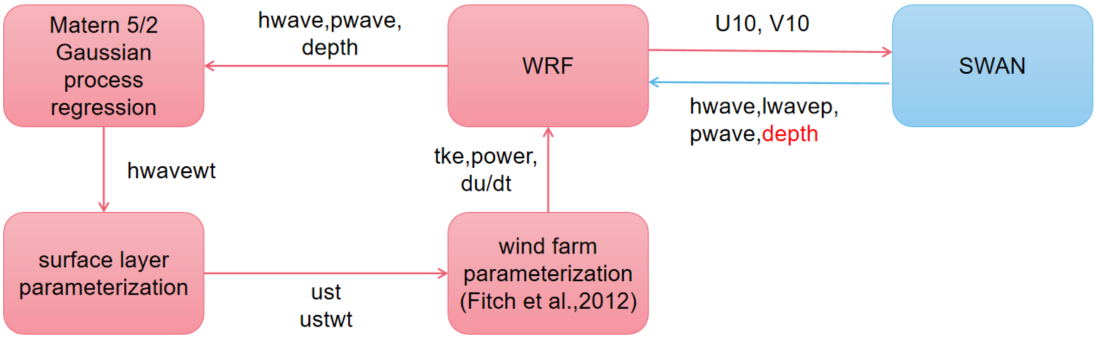

Figure 6. Flow chart of floating offshore wind farms parameterization implemented in the COAWST model

5.2 Model conFigureuration

The new parameterization is tested in the Coupled Ocean-Atmosphere-Wave-Sediment Transport (COAWST) modeling system (Warner et al., 2008; Warner et al, 2010). This coupling system comprises four components, including the atmospheric model (WRF) and the spectral wave model (SWAN), which are connected by The Model Coupling Toolkit (MCT). The other components of COAWST are not activated in this study.

Initial and lateral boundary conditions for the WRF model are obtained from the global forecasting system (GFS) NCEP FNL analysis data with horizontal resolution of 1°. The WRF model has a horizontal grid resolution of 8 km, with the center located at 21.98°N, 115.94°E. There are 275 × 194 grid cells in the horizontal domain (Figure 7a), 47 eta levels in the vertical direction, where 23 levels are below 1000 m and 15 levels intersect the rotor region. The vertical grid spacing at levels spanned by the wind turbine rotor is about 14 m. The major physical parameterization schemes are summarized in Table 1. The wind farm is located in the northern South China Sea at the water depths between 50 and 63 m (Figure 7b). The turbine spacing is about 1 km. The thrust and power coefficients of the LEANWIND 8 MW reference turbine (LW) are presented in Figure 7c. Other main technical parameters of the LW wind turbine are shown in Table. 2 (Desmond et al., 2016).

We use the same model domain and horizontal grid for SWAN as that in the WRF model. The corresponding parameterization schemes are shown in Table 1. The spectrum is discretized using 24 logarithmically-spaced frequency bins from 0.04 to 1.00 Hz and 36 directional bins with 10° spacing. The boundary conditions are taken from the WaveWatch III (WW3) model (WW3DG, 2019). The nonstationary mode of SWAN is used and the effects of quadruplet nonlinear wave-wave interactions are taken into account. In this fully coupled model simulation, SWAN runs with a time step of 60 s, and the WRF model runs with a time step of 36 s. The time interval for data interchange among the models is set to 600 s. The total simulation time is 4 days (i.e., from 00 UTC on 1 January to 00 UTC on 5 January 2019), with SWAN starting from the initial steady state. A reference simulation (control run, referred as WRF-CTL) is performed without the wind farm. Another simulation (WRF-Fitch) is conducted with the Fitch wind farm parameterization. A third simulation (WRF-FWFP) is performed with the new proposed floating wind farm parameterization (FWFP).

Table.1 Major physical parameterization schemes used in COAWST.

	Physics options	Parameterization scheme
WRF	Microphysics	Single-Moment 6-class (Hong & Lim, 2006; Hong et al., 2006)
	Longwave Radiation	Rapid Radiative Transfer Model (Mlawer, 1997)
	Shortwave Radiation	Dudhia (Dudhia, 1989)
	Surface Layer	MYNN (Nakanishi & Niino, 2009)
	Land Surface	thermal diffusion (Duhia, 1996)
	Planetary Boundary Layer	Mellor-Yamada-Nakanishi-Niino 2.5-level (Nakanishi & Niino, 2009)
	Cumulus Parameterization	Grell-Freitas ensemble (Grell & Freitas, 2014)
	Roughness Parameterization	CORE-Talyor-Yelland (Taylor & Yelland, 2001)
SWAN	Depth-induced wave breaking	Constant (1.0, 0.73) (Battjes & Janssen, 1978)
	Bottom friction	Madsen (0.05) (Madsen et al., 1988)
	Wind input	Komen (Komen et al., 1984)
	Whitecapping	Komen (Komen et al., 1984)

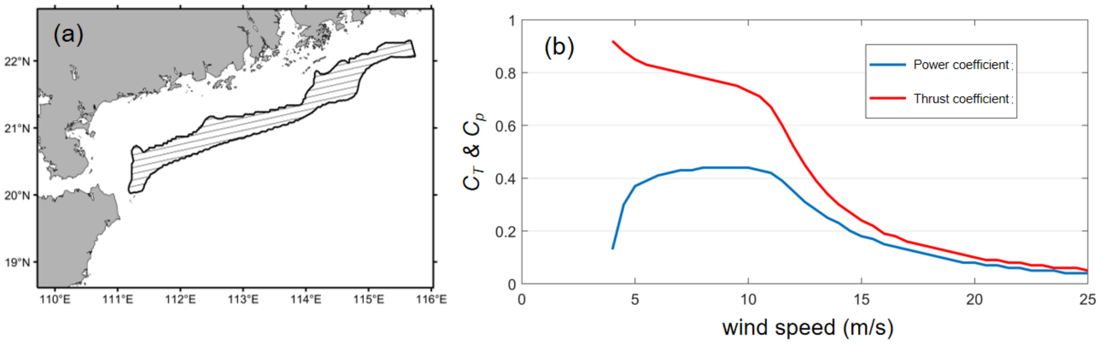

Figure 7. (a) location of wind farm (shaded area), (b) the thrust and power coefficients curves of the LW 8 MW wind turbine

Table.2 Main technical parameters of the LW wind turbine.

Parameters	Value
Rated power	8 MW
Rotor diameter	164 m
Turbine hub height	110 m
Cut in wind speed	4 m/s
Cut out wind speed	25 m/s

5.3 Model validation

To validate SWAN results, the simulated SWH is compared with observations of the satellite data Jason-3 (Lillibridge, 2019) (Figure 8). The model is also run for an additional 2 days for further validation. It is evident that the model generally performs well on the wave simulation for the satellite tracks (Pass 38 and Pass 88). The SWH in the model is a bit underestimated on the track Pass 12 and overestimated on the track Pass 51. Generally, the model results have a reasonable performance.

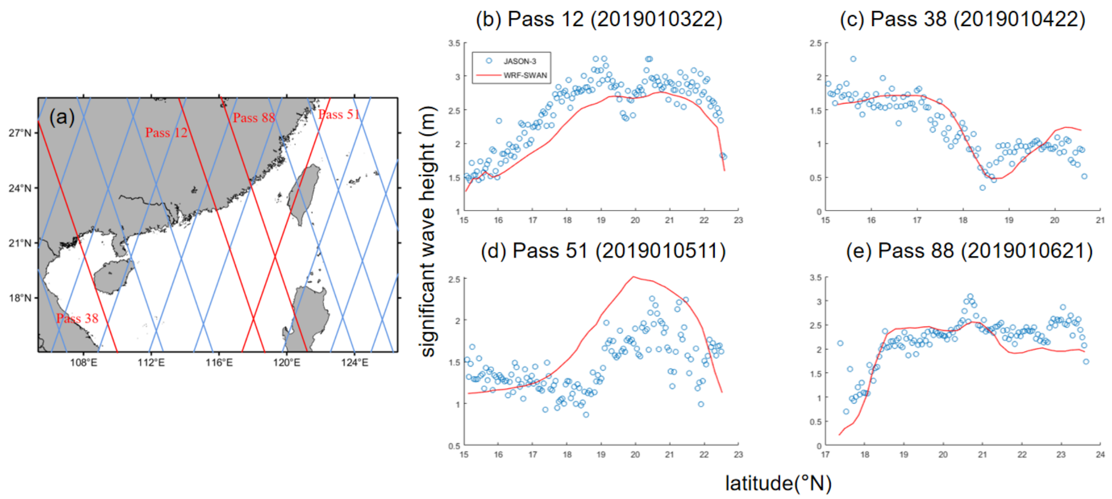

Figure 8. (a) Ground track of the *Jason-3* satellite from 00 UTC on 1 January to 00 UTC on 7 January in the study region. (b) Comparison of SWH between model results and *Jason-3* altimeter data.

5.4 Simulation results

In this section, the differences in power output, wind speed deficits, and TKE between the FWFP and Fitch schemes are analyzed in a realistic case using COAWST.

5.4.1 Power output and wind speed deficits

As the inflow wind speed decreases, the total power output of the experiments is reduced (Figure 9). The total power output of the FWFP scheme can be increased by up to 5.68 GW compared to the Fitch scheme. The relative difference is close to 5% in the high wind speed stage and increases to a maximum of 35% as the wind speed decreases, which is also related to the wind direction. It can also be seen that the power output of the WRF-FWFP is consistently larger than that of the WRF-Fitch, and the horizontal distribution of the difference is presented in the 84 h-averaged results (Figure 9b). FWFP does not directly modify the power output equation in the Fitch scheme. It only modifies momentum tendency terms. However, it should be noted that the change of momentum tendency terms also has a considerable effect on the power output.

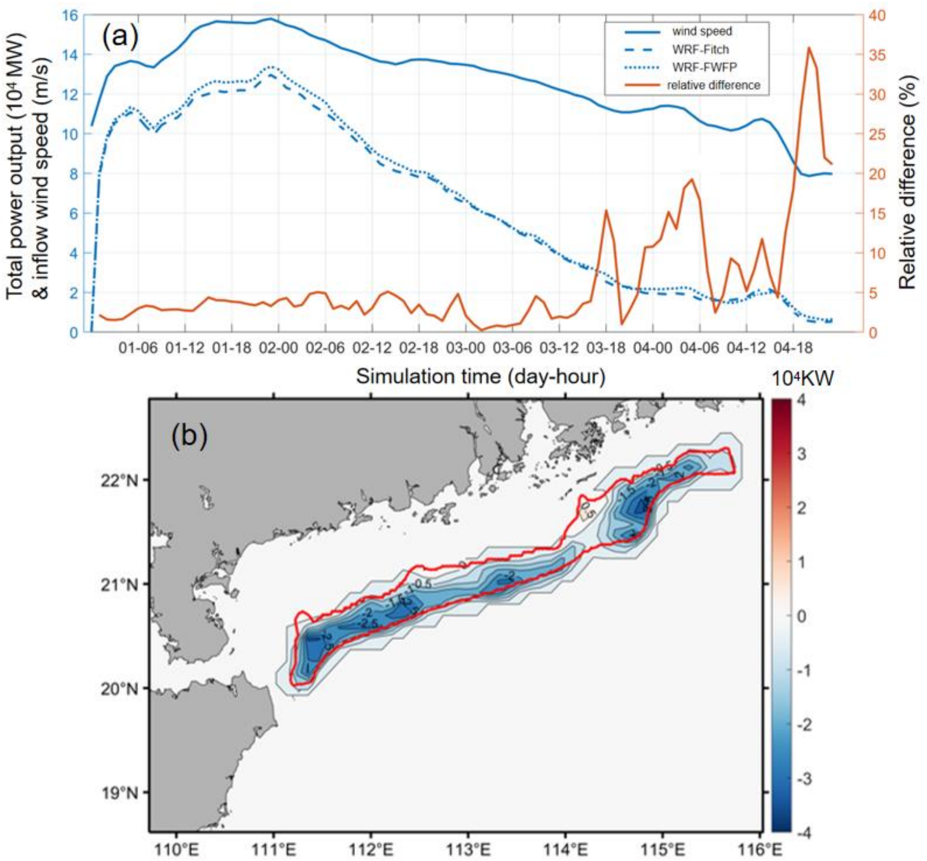

Figure 9. (a) Time series of total power output, inflow wind speed and relative error of total power output. (b) Power output difference is averaged over a period time from 12 UTC on 1 January to 00 UTC on 5 January, and the red solid line indicates the outer boundary of the wind farm.

A small change in wind direction from 12 UTC on 1 January to 18 UTC on 1 January, and this period is after the spin-up of 12 h, so the following analysis is based on this period (Figure 10). The FWFP scheme reduces the momentum with a maximum value of 6.5 m/s, which is a reduction 43% at the hub height level (Figure 11a). Behind the wind farm, the wind speed deficit extends a long wake. A 2 m/s (13%) deficit reaches 60 km from the downstream edge of the wind farm (20.03°N, 111.19°E). Previous studies found that wakes behind offshore wind turbines and farms are expected to be much longer than behind onshore wind turbines and farms due to the smaller aerodynamic roughness length and turbulence intensity (~50 km) (Emeis et al., 2016; Lundquist et al., 2019). We find that the wind speed deficit at hub height in the WRF-Fitch case is larger than that of the WRF-FWFP (Figure 11b), which helps to explain why the power output is greater in our FWFP scheme. Eq. (21) indicates that the FWFP takes into account the fact that the frictional velocities at the turbine locations are lower at this moment. The FWFP also has a slight impact on the wind-farm wakes.

Vertical profiles of wind speed deficits in WRF-FWFP case also show similar characteristics to WRF-Fitch case. The wind farm induces a maximum wind speed deficit of up to 5 m/s at the hub height, and the wind speed deficit spreads throughout the atmospheric boundary layer (ABL), including downstream of the wind farm (Figure 12a). A wind speed deficit of 1 m/s can extend up to the top of the ABL. Figure 12b shows the clear differences that occur within the wind farm, with the Fitch scheme overestimating the wind speed deficit within the ABL compared to the FWFP scheme, which is most pronounced in the rotor area with a maximum value of 0.6 m/s. The top of the turbine to the top of the ABL and the wind-farm wakes also have an effect with values of 0.1 to 0.2 m/s. The difference between the two schemes decreases rapidly at heights above the top of the turbine (sparsity in the contours).

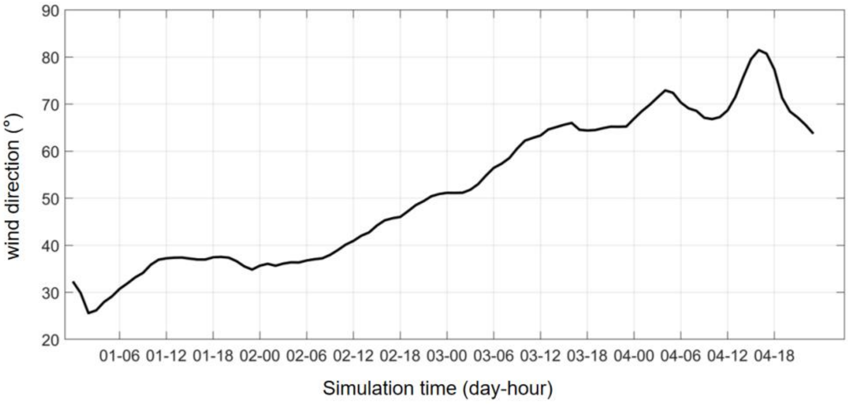

Figure 10. Time series of wind direction at hub height within the wind farm (northerly wind direction is 0° and easterly wind direction is 90°)

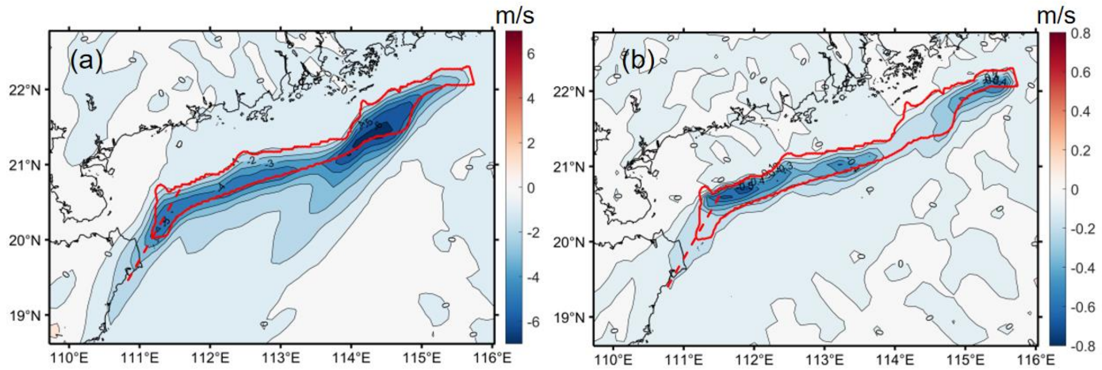

Figure 11. Horizontal wind speed differences at the hub height level between (a) WRF-FWFP and WRF-CTL cases and (b) WRF-Fitch and WRF-FWFP cases, averaged from 12 UTC on 1 January to 18 UTC on 1 January. The red solid line indicates the outer boundary of the wind farm, and the dashed red lines indicate a cross section analyzed further.

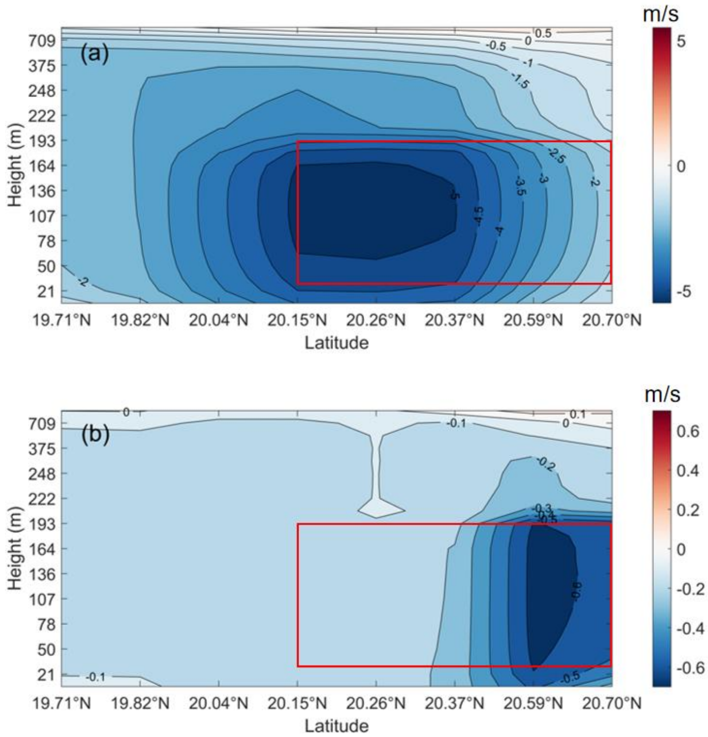

Figure 12. Vertical transect of the wind speed differences between (a) WRF-FWFP and WRF-CTL cases and (b) WRF-Fitch and WRF-FWFP cases, averaged from 12 UTC to 18 UTC on 1 January along the dashed red lines in Figure 11. The red solid lines indicate the rotor area.

5.4.2 TKE

The generation of TKE within the wind farm is largely restricted to the farm area, and decays rapidly downstream despite the advection of TKE. A maximum increase of TKE of 2.4 m^2s^{-2} at the top of the turbine is seen within the wind farm (Figure 13a). The WRF-FWFP case produces a smaller TKE within the wind farm compared to the WRF-Fitch case, with a maximum reduction of 0.8 m^2s^{-2} (Figure 13b). The distribution of horizontal TKE differences is highly similar to that of horizontal wind speed differences (Figure 11b), indicating that the wind shear may dominate the TKE distribution. The reduction in the TKE of 0.3 m^2s^{-2} continues to extend more than 80 km downstream near the surface (Figure 13c). However, there is little difference in between the WRF-Fitch and the WRF-FWFP in the downstream near the surface (Figure 13d), with most of differences occurring only within the wind farm. The reduction in TKE near the surface in the downstream in WFP-Fitch (Figure 13c) is due to a wind speed deficit and a corresponding reduction in wind shear in the lower levels of the wake, resulting in a decrease in shear production in TKE and the reduction in the TKE is no higher than at the top of the turbine (Fitch et al., 2012).

As the wind speed deficits, the increase in TKE spreads to the top of the ABL which is above the wind farm, with a rise of 0.3 m^2s^{-2} reaching a height of nearly 709 m (Figure 14a). At the top of the turbine, the maximum increase in TKE is 2.4 m^2s^{-2}. Above the top of the turbine, the increase in TKE decreases with height, and below the top of the turbine it increases with height. The difference in TKE between the WRF-Fitch and the WRF-FWFP appears within the local wind farm and is consistent with the location of the difference in wind speeds (Figure 14b). Compared to the WRF-FWFP, WRF-Fitch overestimates the TKE generated throughout the ABL, with the TKE at the top of the wind turbine being the most overestimated (0.4 m^2s^{-2}).

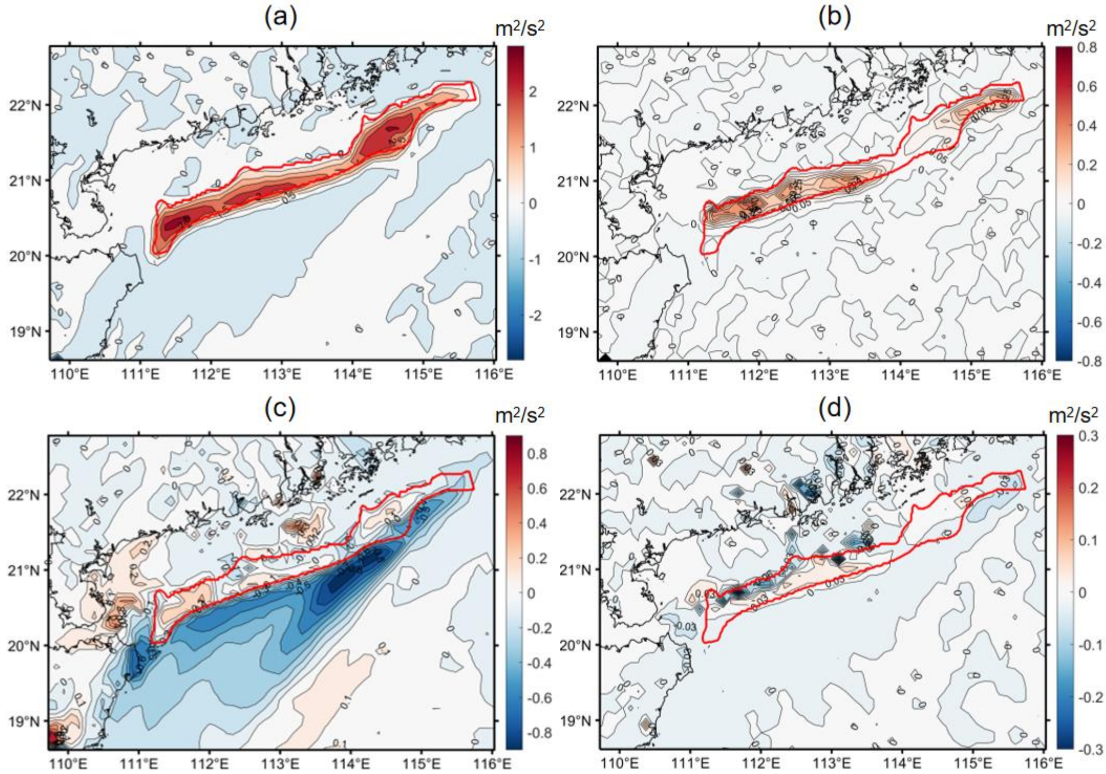

Figure 13. Horizontal TKE differences at the top of the turbine between (a) WRF-FWFP and WRF-CTL cases and (b) WRF-Fitch and WRF-FWFP cases, near the surface between (c) WRF-FWFP and WRF-CTL cases and (d) WRF-Fitch and WRF-FWFP cases, averaged from 12 UTC on 1 January to 18 UTC on 1 January, and the red solid line shows the outer boundary of the wind farm

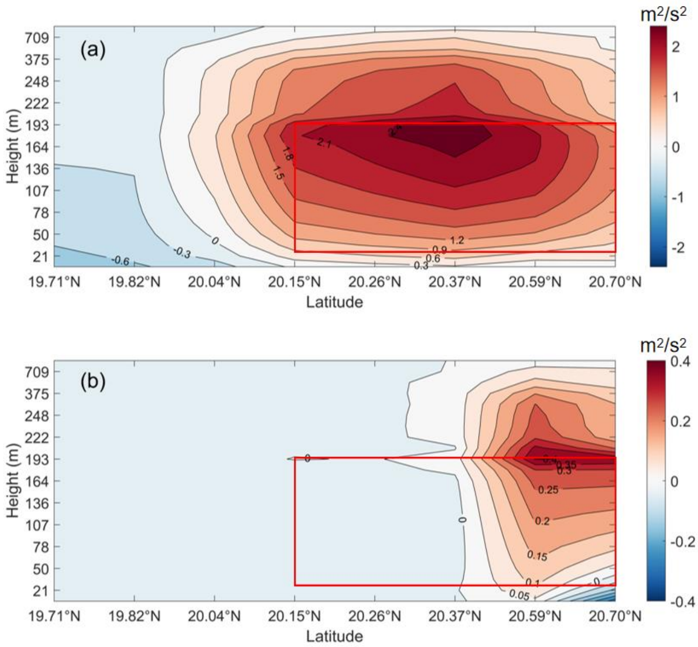

Figure 14. The same as in Figure 12, but for TKE

The TKE budget is then examined. The TKE per unit mass, expressed as $q^2/2$ in the MYNN model, is predicted by the following equation for a dry atmosphere:

$$\frac{\mathrm{d}(q^2/2)}{\mathrm{d}t} = P_s + P_b + P_v + P_d \tag{22}$$

where P_s is the shear production term, P_b is the buoyancy production term, P_v is the vertical transport and pressure distribution term, and P_d is the dissipation term. The details about the equations can refer to Janji (2001).

The largest source of the difference in TKE at the top of the turbine is shear generation (Figure 15a), with the TKE at 235 m still making a positive contribution to this difference through vertical transport. The other source is dissipation term, which is the major source of TKE differences in the rotor area. The variation in TKE near the surface within the wind farm is more complex, with the shear production term, the vertical transport term, and the dissipation term all being important sources, while the production of TKE by buoyancy is negligible compared with the other terms (not shown). At the location of 20.59°N, 111.57°E, the vertical shear of the wind speed is not only the largest at the top of the turbine for both WRF-Fitch and the WRF-FWFP, but the difference between the two cases is also the greatest at the top of the turbine (Figure 16). Specifically, the wind shear is 0.056 s^{-1} for WRF-Fitch and 0.0446 s^{-1} for WRF-FWFP. This result can actually be inferred from Figure 12b, which shows that although the maximum value of the difference in wind speed deficit between the two cases is in the rotor area, this difference varies slightly with height, and the height at which the variation with height is most pronounced is at the top of the turbine, followed by the bottom of the rotor area. The smaller wind shear results in the smaller TKE.

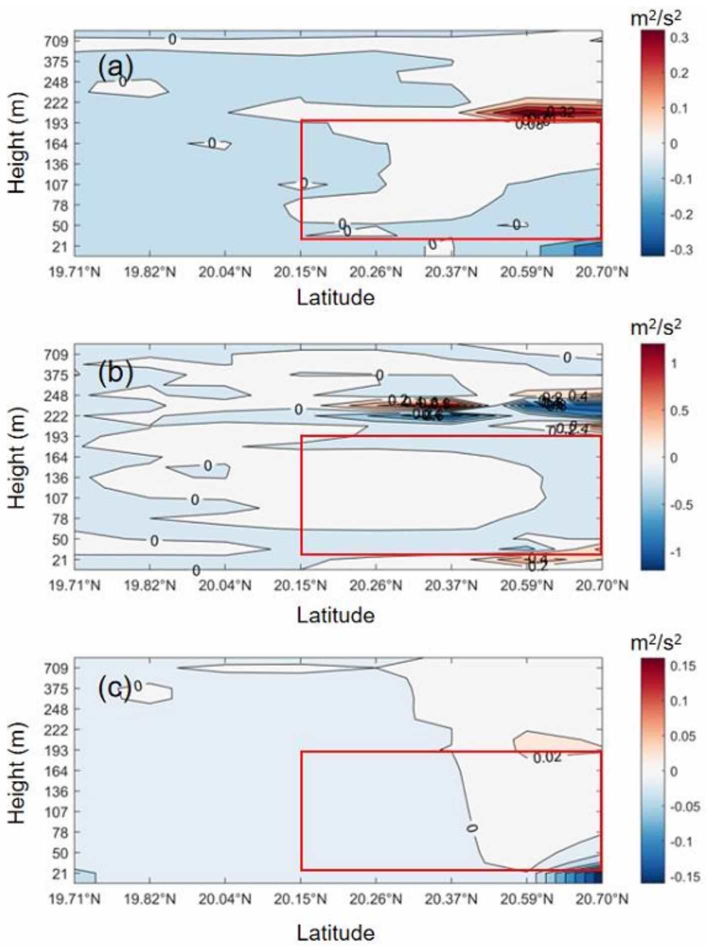

Figure 15. Vertical transect of the differences in the TKE budget components between WRF-Fitch and WRF-FWFP cases: (a) shear generation (b) vertical transport (c) dissipation, averaged from 12 UTC on 1 January to 18 UTC on 1 January along the dashed red lines in Figure 11a and 11c. The red solid line indicates the rotor area.

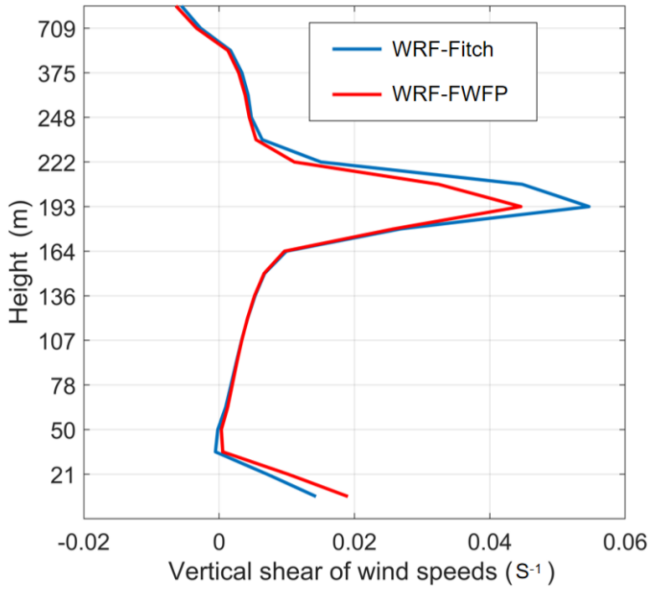

Figure 16. Profile of the vertical shear of wind speeds at the location 20.59°N, 111.57°E, averaged from 12 UTC on 1 January to 18 UTC on 1 January

6. Conclusions and discussion

Parameters of the column is modified in the VEG module of SWAN to include the effect of the inertial force to make it suitable for the application of the side column of a floating offshore wind turbine. At the same time, a series of idealized high-resolution SWAN simulations are conducted to investigate the dissipation of wave energy induced by the side columns of floating turbines. It is found that under certain conditions, the side columns of floating turbines can attenuate more than 50% of the significant wave height (SWH), and a wave "wake" phenomenon occurs with a recovery length of ~1 km. The mean wave direction is also affected, with a symmetrical change of about 5° around the side columns, and the mean wave length increases by more than 20 m. The idealized SWAN simulations and theoretical analyses show that the attenuation of the SWH becomes smaller with the increase of the water depth and is enhanced with the increase of the peak wave period. A total of 660 groups of experiments consisting of different incident SWHs, water depths, and peak wave periods are conducted, and the results of these idealized simulations are used to train a Gaussian process regression (GPR) model with the Matern 5/2 kernel. This model can predict the attenuated SWH due to the side columns of the floating turbine with a given water depth, peak wave period, and incident SWH.

The GPR model is implemented in the WRF and the Fitch wind farm parameterization scheme is modified to form a floating wind farm parameterization scheme (FWFP). The FWFP modifies the equations for the momentum tendency term because floating structures affect SWH, then the momentum tendency term must also account for changes in surface layer momentum fluxes due to changes in SWH. The difference of the results between the original Fitch scheme and our new FWFP scheme is analyzed in a realistic simulation using a coupled atmosphere-wave model.

Compared with the Fitch scheme, the FWFP scheme increases the total power output with a maximum increase of ~5.68 GW. The relative difference is close to 5% in the high wind speed stage. This is due to the fact that the FWFP scheme takes into account the change in roughness of ocean surface, the Fitch scheme overestimates the wind speed deficit within the wind farm. The impacts spread to the atmospheric boundary layer (ABL) and the wakes, but are most pronounced in in the rotor area, which can be up to 0.6 m/s, suggesting a 15 to 24% reduction in wind speed deficits. The impact of the FWFP on the turbulent kinetic energy (TKE) near the surface in the downstream of the wind farm is marginal, and it mainly influences the TKE within the wind farm (including the ABL). The Fitch scheme overestimates the TKE generation compared to the FWFP scheme, with the maximum value of 0.4 m^2s^{-2} overestimated at the top of the turbine. Because the FWFP diminishes the vertical wind shear at the top of the turbine, which in turn reduces the TKE generated.

Note that a decrease in SWH does not necessarily increase the wind speed in surface layer. In this study, we chose the roughness length parameterization scheme proposed by Taylor & Yelland. (2001), which is a complex iterative computational method where the frictional velocity and roughness length are dependent on each other. The FWFP scheme is only applicable to semi-submersible floating wind turbines because the wind turbine occupying a larger area can induce a significant change in roughness length. In contrast to most sites onshore, the roughness length of the surface offshore is not static, but changes dynamically with sea state. In order to better evaluate the power output of offshore wind farms and their impacts on the environment, it is necessary to improve the offshore wind farms parameterization.

Data availability statement

The NCEP FNL analysis can be download for free at website https://rda.ucar.edu/datasets/ds083.0/ (NECP, 1999) [Dataset], WW3 can be download at https://www.ncei.noaa.gov/thredds-ocean/catalog/ncep/nww3/catalog.html (WW3DG, 2019), and Jason-3 can be obtained from https://www.ncei.noaa.gov/products/jason-satellite-products (Lillibridge, 2019). COAWST is freely available online (https://github.com/DOI-USGS/COAWST) (Warner et al., 2010).

Acknowledgements

This study is supported by funds from Shenzhen Science and Technology Innovation Committee (WDZC20200819105831001) and the Guangdong Basic and Applied Basic Research Foundation (2022B1515130006). SC is also supported by the Scientific Research Start-up Fund (QD2021021C).

References

Abkar, M., & Porté-Agel, F. (2015), A new wind-farm parameterization for large-scale atmospheric models. *Journal of Renewable and Sustainable Energy*, *7*(1), 013121. https://doi.org/10.1063/1.4907600

Alari, V., & Raudsepp, U. (2012). Simulation of wave damping near coast due to offshore wind farms. *Journal of Coastal Research*, *279*(1), 143–148. https://doi.org/10.2037/41331997

AlSam, A., Szasz, R., Revstedt, J. (2015). The influence of sea waves on offshore wind turbine aerodynamics. *Journal of Energy Resources Technology, Transactions of the ASME, 137*(5), 1-10. https://doi.org/10.1115/1.4031005

Battjes, J., & Janssen, J. (1978). Energy loss and set-up due to breaking of random waves. C*ostal Engineering Proceedings*, *1*(16), 32. https://doi.org/10.9753/icce.v16.32

Blahak, U., Goretzki, B., & Meis, J. (2010). A simple parameterization of drag forces induced by large wind farms for numerical weather prediction models. E*uropean Wind Energy Conference and Exhibition 2010 EWEC, 6*(1), 4577–4585.

Booij, N., Ris, R., & Holthuijsen, L. (1999). A third-generation wave model for coastal regions: 1. model description and validation. *Journal of Geophysical Research: Atmospheres, 104*(4), 7649-7666. https://doi.org/10.1029/98JC02622

Christensen, E., Johnson, M., Sørensen, O., Hasager, C., Badger, M., & Larsen, S. (2013). Transmission of wave energy through an offshore wind turbine farm. *Coastal Engineering ,82*, 25-46. https://doi.org/10.1016/j.coastaleng.2013.08.004

Dalrymple, R., Kirby, J., & Hwang, P. (1984). Wave diffraction due to areas of energy dissipation. *Journal of Waterway, Port, Coastal and Ocean Engineering*, *110*(1), 67-79. https://doi.org/10.1061/(ASCE)0733-950X(1984)110:1(67)

Desmond, C., Murphy, J., Blonk, L., & Haans, W. (2016). Description of an 8 MW reference wind turbine. *Journal of Physics Conference Series*, *753*(9), 092013. https://doi.org/10.1088/1742-6596/753/9/092013

Diaz, H., & Guedes Soares, C. (2020). Review of the current status, technology and future trends of offshore wind farms. *Ocean Engineering, 209,* 107381. https://doi.org/10.1016/j.oceaneng.2020.107381

Du, J., Bolanos, R., & Guo Larsen, X. (2017). The use of wave boundary layer model in SWAN. *Journal of Geophysical Research: Oceans*, *122*(1):42-62. https://doi.org/10.1002/2016JC012104

Dudhia, J. (1989). Numerical study of convection observed during the winter monsoon experiment using a mesoscale two-dimensional model. *Journal of Atmospheric Sciences*, *46*(20), 3077-3107. https://doi.org/10.1175/1520-0469(1989)046<3077:NSOCOD>2.0.CO;2

Dudhia, J. (1996). A multi-layer soil temperature model for MM5. Sixth PSU/NCAR Mesoscale Model Users Workshop 1996, Boulder, CO, PSU/NCAR, 4950.

Emeis, S. (2010). A simple analytical wind park model considering atmospheric stability. *Wind Energy ,13*, 459-469. https://doi.org/10.1002/we.367

Emeis, S., Siedersleben, S., Lampert, A., Platis, A., Bange, J., Djath, B., et al. (2016). Exploring the wakes of large offshore wind farms. *Journal of Physics Conference Series*, *753*(9), 092014. https://doi.org/10.1088/1742-6596/753/9/092014

Fitch, A., Olson, J., Lundquist, J., Dudhia, J., Gupta, A., Michalakes, J., et al. (2012). Local and mesoscale impacts of wind farms as parameterized in a mesoscale NWP Model. *Monthly Weather Review, 140*(9), 3017-3038. https://doi.org/10.1175/MWR-D-11-00352.1

Fitch, A., Olson, J., & Lundquist, J. (2013). Parameterization of wind farms in climate models. *Journal of Climate, 26,* 6439–6458. https://doi.org/10.1175/JCLI-D-12-00376.1

Fitch, A. (2015). Climate impacts of large-scale wind farms as parameterized in a global climate model. *Journal of Climate, 28,* 6160-6180. https://doi.org/10.1175/JCLI-D-14-00245.1

Gettelman, A., Gagne, D., Chen, C., Christensen, M., Lebo, Z., Morrison, H., et al. (2020). Machine learning the warm rain process. *Journal of Advances in Modeling Earth Systems, 13*(2), e2020MS002268. https://doi.org/10.1029/2020MS002268

Grell, G., & Freitas, S. (2013). A scale and aerosol aware stochastic convective parameterization for weather and air quality modeling. *Atmospheric Chemistry and Physics*, *13*(9), 5233-5250. https://doi.org/10.5194/acpd-13-23845-2013

Holthuijsen, L., Herman, A., & Booij, N. (2003). Phase-decoupled refraction-diffraction for spectral wave models. *Coastal Engineering, 49*(4), 291-305. https://doi.org/10.1016/S0378-3839(03)00065-6

Hong, S., & Lim, J. (2006). WRF single-moment 6-class microphysics scheme (WSM6). *Journal of the Korean Meteorological Society, 42,*129-151.

Hong, S., Noh, Y., & Dudhia, J. (2006). A new vertical diffusion package with an explicit treatment of entrainment processes. *Monthly Weather Review, 134,* 2318-2341. https://doi.org/10.1175/MWR3199.1

Isaacson, M. (1979). Wave-induced forces in the diffraction regime. In: Shwa T L, ed. Mechanics of wave-induced forces on cylinders. London: Pitman Publishing, 68-89.

Janjic, Z. (2001). Nonsingular implementation of the Mellor-Yamada level 2.5 scheme in the NCEP Meso model. NCEP Office note #437 2001;61.

Jenkins, A., Paskyabi, M., Fer, I., Gupta, A., & Adakudlu, M. (2012). Modelling the effect of ocean waves on the atmospheric and ocean boundary layers. *Energy Procedia, 24*, 166-175. https://doi.org/10.1016/j.egypro.2012.06.098

Kalvig, S., Manger, E., Hjertager, B., & Jakobsen, J. (2014). Wave influenced wind and the effect on offshore wind turbine performance. *Energy Procedia*, *53*, 202-213. https://doi.org/10.1016/j.egypro.2014.07.229

Kobayashi, N., Raichle, A., & Asano, T. (1993). Wave attenuation by vegetation. *Journal of Waterway, Port, Coastal and Ocean Engineering, 119*(1), 30-48. https://doi.org/10.1061/(ASCE)0733-950X(1993)119:1(30)

Komen, G., Hasselmann, S., & Hasselmann, K. (1984). On the existence of a fully developed wind-sea spectrum. *Journal of Physical Oceanography*, *14*(8), 1271-1285. https://doi.org/10.1175/1520-0485(1984)014<1271:OTEOAF>2.0.CO;2

Lillibridge, John; US DOC/NOAA/NESDIS > Office of Satellite Data Processing and Distribution (2019). Jason-3 Level-2 Operational, Interim and Final Geophysical Data Records (X-GDR), 2016 to present (NCEI Accession 0122595).

Lundquist, J., DuVivier, K., Kaffine, D., & Tomaszewski, J. (2019). Costs and consequences of wind turbine wake effects arising from uncoordinated wind energy development. *Nature Energy*, *4*(1), 26-34. https://doi.org/10.1038/s41560-018-0281-2

Madsen, O., Poon, Y., & Graber, H. (1988). Spectral wave attenuation by bottom friction: Theory. Proceedings of the 21st International Conference Coastal Engineering, 492-504.

McCombs, M., Mulligan, R., & Boegman, L. (2014). Offshore wind farm impacts on surface waves and circulation in Eastern Lake Ontario. *Coastal Engineering*, 93, 32-38. https://doi.org/10.1016/j.coastaleng.2014.08.001

Mendez, F., & Losada, I. (2004). An empirical model to estimate the propagation of random breaking and nonbreaking waves over vegetation fields. *Coastal Engineering, 51* (2), 103-118. https://doi.org/10.1016/j.coastaleng.2003.11.003

Mlawer, E., Taubman, S., Brown, P., Iacono, M., & Clough, S. (1997). Radiative transfer for inhomogeneous atmospheres: RRTM, a validated correlated-k model for the longwave. *Journal of Geophysical Research: Atmospheres, 102*, 16663–16682. https://doi.org/10.1029/97JD00237

Molen, J., Smith, H., Lepper, P., Limpenny, S., & Rees, J. (2014). Predicting the large-scale consequence of offshore wind turbine array development on a North Sea ecosystem. *Continental Shelf Research*, *85*, 60-72. https://doi.org/10.1016/j.csr.2014.05.018

Morison, J., Johnson, J., & Schaaf, S. (1950). The force exerted by surface waves on piles. Journal of Petroleum Technology, 2(5), 149-154. https://doi.org/10.2118/950149-G

Nakanishi, M., & Niino, H. (2009). Development of an improved turbulence closure model for the atmospheric boundary layer. *Journal of the Meteorological Society of Japan Ser, 87*(5), 895-912. https://doi.org/10.2151/jmsj.87.895

NCEP. (1999). FNL operational model global tropospheric analyses [Dataset]. NCEP. Retrieved from https://rda.ucar.edu/datasets/ds083.0

O'Gorman, P., & Dwyer, J. (2018). Using machine learning to parameterize moist convection: Potential for modeling of climate, climate change, and extreme events. *Journal of Advances in Modeling Earth Systems*, *10*(10), 2548-2563. https://doi.org/10.1029/2018MS001351

Pan, Y., & Archer, C. (2018). A hybrid wind-farm parametrization for mesoscale and climate models. *Boundary-Layer Meteorology*, *168*(3), 469-495. https://doi.org/10.1007/s10546-018-0351-9

Paskyabi, M., Zieger, S., Jenkins, A., Babanin, A., & Chalikov, D. (2014). Sea surface gravity wave-wind interaction in the marine atmospheric boundary layer. *Energy Procedia*, *53*, 184-192. https://doi.org/10.1016/j.egypro.2014.07.227

Ponce de León, S., Bettencourt, J., & Kjerstad, N. (2011). Simulation of irregular waves in an offshore wind farm with a spectral wave model. *Continental Shelf Research*, *31*, 1541-1557. https://doi.org/10.1016/j.csr.2011.07.003

Porchetta, S., Munoz-Esparza, D., Munters, W., Beeck, J., & Lipzig, N. (2021). Impact of ocean waves on offshore wind farm power production. *Renewable Energy, 180*, 1179-1193. https://doi.org/j.renene.2021.08.111

Redfern, S., Olson, J., Lundquist, J., & Clack, C. (2019). Incorporation of the rotor-equivalent wind speed into the weather research and forecasting model's wind farm parameterization. *Monthly Weather Review*, *147*(3), 1029-1046. https://doi.org/10.1175/MWR-D-18-0194.1

Roddier, D., Cermelli, C., Aubault, A., & Weinstein A. (2010). Wind Float: A floating foundation for offshore wind turbines. *Journal of Renewable and Sustainable Energy, 2*(3), 033104. https://doi.org/10.1063/1.3435339

Seifert, A., & Rasp, S. (2020). Potential and limitations of machine learning for modeling warm-rain cloud microphysical processes. *Journal of Advances in Modeling Earth Systems*, 12(12), e2020MS002301. https://doi.org/10.1029/2020MS002301

Siedersleben, S., Lundquist, J., Platis, A., Bange, J., Barfuss, K., & Lampert, A., et al. (2018). Micrometeorological impacts of offshore wind farms as seen in observations and simulations. *Environmental Research Letters, 13*(12), 124012. https://doi.org/10.1088/1748-9326/aaea0b

Taylor, P., & Yelland, M. (2001). The dependence of sea surface roughness on the height and steepness of the waves. *Journal of Physical Oceanography, 31*(2), 572-590. https://doi.org/10.1175/1520-0485(2001)031<0572:TDOSSR>2.0.CO;2

The SWAN team.(2023). SWAN Scientific and Technical Documentation version 41.45.

Vanderwende, B., & Lundquist, J. (2016). Could crop height affect the wind resource at agriculturally productive wind farm sites? *Boundary-Layer Meteorology, 158*(3), 409-428. https://doi.org/10.1007/s10546-015-0102-0

Volker, P., Badger, J., Hahmann, A., & Ott, S. (2015). The explicit wake parametrization V1.0: a wind farm parametrization in the mesoscale model WRF. *Geoscientific Model Development, 8*(11), 3715-3731. https://doi.org/10.5194/gmd-8-3175-2015

Warner, J., Sherwood, C., Signell, R., Harris, C., & Arango, H. (2008). Development of a three-dimensional, regional, coupled wave, current and sediment transport model. *Computers & Geosciences, 34*(10), 1280-1306. https://doi.org/10.1016/j.cageo.2008.02.012

Warner, J., Armstrong, B., He, R., & Zambon, J. (2010). Development of a coupled ocean-atmosphere-wave-sediment transport (COAWST) modeling system. *Ocean Modelling, 35* (3), 230-244. https://doi.org/10.1016/j.ocemod.2010.07.010

WW3DG, W. I. D. G. (2019). User manual and system documentation of Wavewatch III (R) version 6.07.

Wu, L., Shao, M., & Sahlée, E. (2020). Impact of air-wave-sea coupling on the simulation of offshore wind and wave energy potentials. *Atmosphere, 11*(4), 327. https://doi.org/10.3390/atmos11040327

Yang, D., Meneveau, C., & Shen, L. (2014). Effect of downwind swells on offshore wind energy harvesting-A large-eddy simulation study. *Renewable Energy, 70*, 11-23. https://doi.org/10.1016/j.renene.2014.03.069

Zou, Z., Zhao, D., Zhang, J., Li, S., Cheng, Y., Lv, H., et al. (2018). The influence of swell on the atmospheric boundary layer under nonneutral conditions. *Journal of Physical Oceanography, 48*(4), 925-936. https://doi.org/10.1175/JPO-D-17-0195.1